Prof. G. A. Brown	Dr. J. B. Heywood	M. A. Lutz
Prof. R. S. Cooper	R. Dethlefsen	C. A. McNary
Prof. W. H. Heiser	K. R. Edwards	P. Ponthus
Prof. M. A. Hoffman	W. Engelmaier	R. P. Porter
Prof. W. D. Jackson	J. W. Gadzuk	D. S. Shupe
Prof. J. L. Kerrebrock	T. K. Gustafson	C. V. Smith, Jr.
Prof. J. E. McCune	A. S. Kalelkar	A. Solbes
Prof. G. C. Oates	R. F. Keating	R. J. Thome
Prof. E. S. Pierson	G. B. Kliman	J. C. Wissmiller
Prof. A. H. Shapiro	A. G. F. Kniazzeh	S. Yamamoto
Prof. R. E. Stickney	R. M. Logan	G. W. Zeiders
	B. T. Lubin	

A. STEAM-WATER CONDENSING EJECTOR TEST FACILITY

The use of a condensing ejector in a liquid-metal MHD power system has been pre-viously reviewed by Brown.[1] Even though experimental performance data[2,3] for a steam-water condensing ejector has demonstrated the feasibility of obtaining exit stag-nation pressures greater than either of the inlet stagnation pressures, data are lacking in the range of high area contraction ratios, high inlet vapor velocities and low flow-rate ratios. Brown has reviewed the need for these conditions in order to obtain high effi-ciency performance (based on an availability definition) from a condensing ejector. Thus, as previously reported,[1] a steam-water test facility was constructed to operate with the flow, geometry, and thermodynamic conditions required to yield operating efficiencies for a condensing ejector in the 60-70 per cent range.

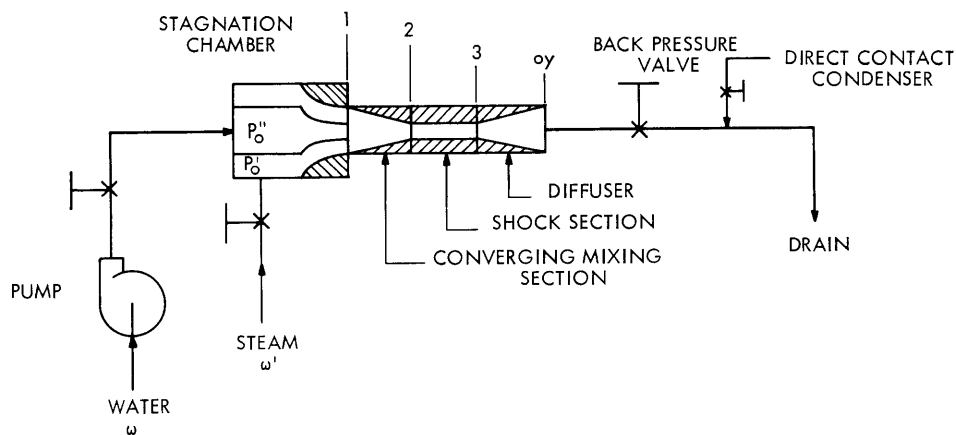The facility is represented schematically in Fig. XII-1.

Fig. XII-1. Schematic diagram of the condensing ejector test facility.

The facility has been designed with a large amount of flexibility so that both inlet and test sections can be replaced with a minimum of difficulty. Stagnation-pressure operation will be 50-180 psia, with a design flow-rate ratio of 2.73 and an area contraction ratio (A_1/A_2) of 11.0. Exit pressures (P_{0y}) of 400-800 psia should be theoretically obtainable.

In order to check out the facility, the previous tests[2] were repeated. The results of the new series of tests are shown in Fig. XII-2, in which the data of the other tests are included. These data cover a range liquid-to-steam flow ratio from 12 to 6.8. Figure XII-3 shows a comparison between the theoretical calculations for (P_{0y}/P_0'') and the experimental values obtained from the present facility. Agreement is within 10 per cent.
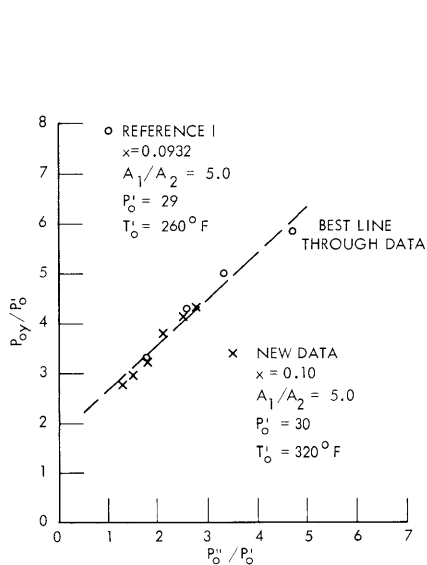

Fig. XII-2.

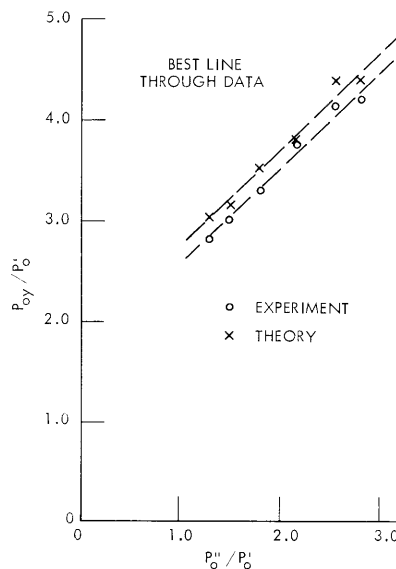Experimental data: Exit stagnation pressure ratio vs inlet stagnation pressure ratio.

Fig. XII-3.

Theory and experiment: Exit stagnation pressure ratio vs inlet stagnation pressure ratio.

Our immediate concern in the test program is to improve the comparison between theoretical and experimental flow rates, as well as to carry out an enthalpy balance on the facility. Subsequent tests will then be undertaken with a test section having higher contraction ratio geometry and lower flow-rate ratios.

B. T. Lubin, G. A. Brown

References

1. G. A. Brown, "Magnetohydrodynamic Power Generation with Liquid Metals," Quarterly Progress Report No. 76, Research Laboratory of Electronics, M. I. T., January 15, 1965, pp. 149-153.

2. G. A. Brown, "An Analysis of NUOS Condensuctor Test Data with a New Theory for the Variable Area Condensuctor," Report 44, Joseph Kaye and Company, Inc., Cambridge, Mass., 1961.

3. J. Miguel and G. A. Brown, "An Analytical and Experimental Investigation of a Condensing Ejector with a Condensable Vapor," AIAA Paper 64-469, July 1964.

B. MAGNETOHYDRODYNAMIC CHANNEL FLOW VELOCITY PROFILES
   AND ENTRY LENGTH

Preliminary experiments were conducted with magnetohydrodynamic (MHD) channel
flows to determine MHD entry lengths from pitot tube measurements of velocity profiles.
The entry length — the length of flow in a magnetic field region required for full profile
development — is important in the design of MHD power-generating equipment and in the
interpretation of MHD friction factor measurements.

The pitot tube (length 0. 9 inch, tip diameter 0. 028 inch) shown in Fig. XII-4 was
traversed across the 0. 5-cm height of a 0. 5 × 5 cm stainless-steel rectangular channel
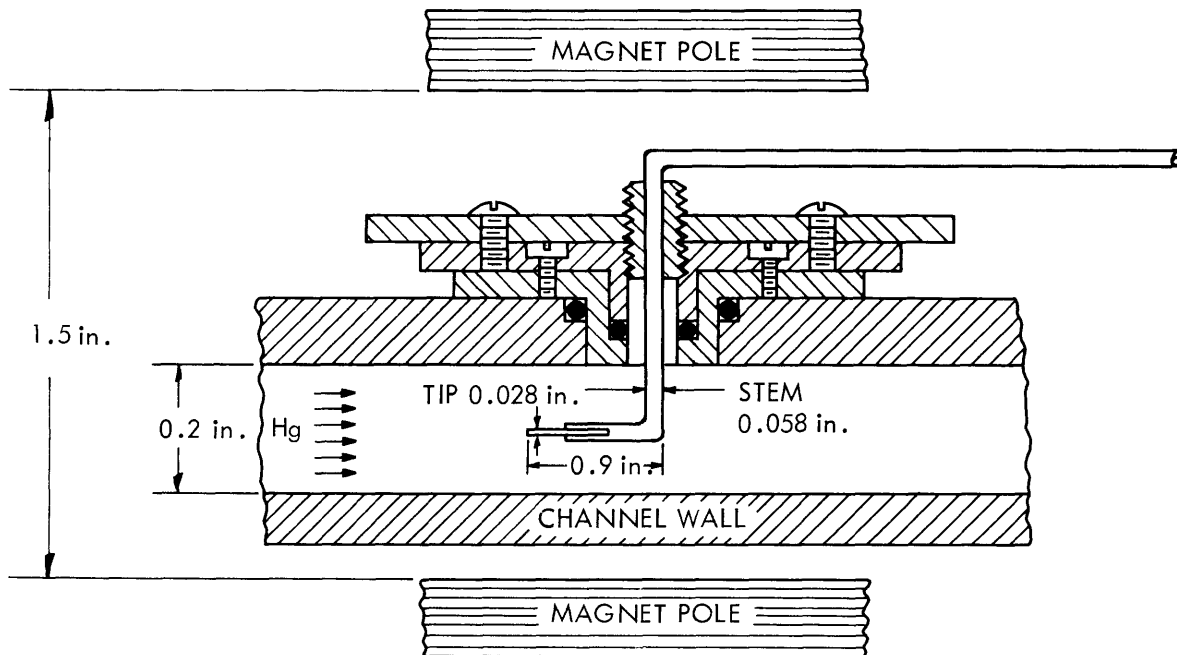

Fig. XII-4. Cross-section view of the pitot tube apparatus.

at a point 50 hydraulic diameters downstream of the channel entrance and 35 hydraulic
diameters upstream of the exit. A magnet of length equivalent to 20 hydraulic diameters
of the channel was located at several positions relative to the pitot tube as shown in
Fig. XII-5. Velocities were computed from pressure measurements by using Bernoulli's
equation.[1]

Figure XII-5 is a record of MHD profile development. At an approximately constant
Reynolds number the velocity profile (drawn on an expanded scale) flattens as the field
is brought from downstream of the pitot tube to a location where the field interacts with
the fluid before the fluid reaches the pitot tube. In this flow an approximately fully
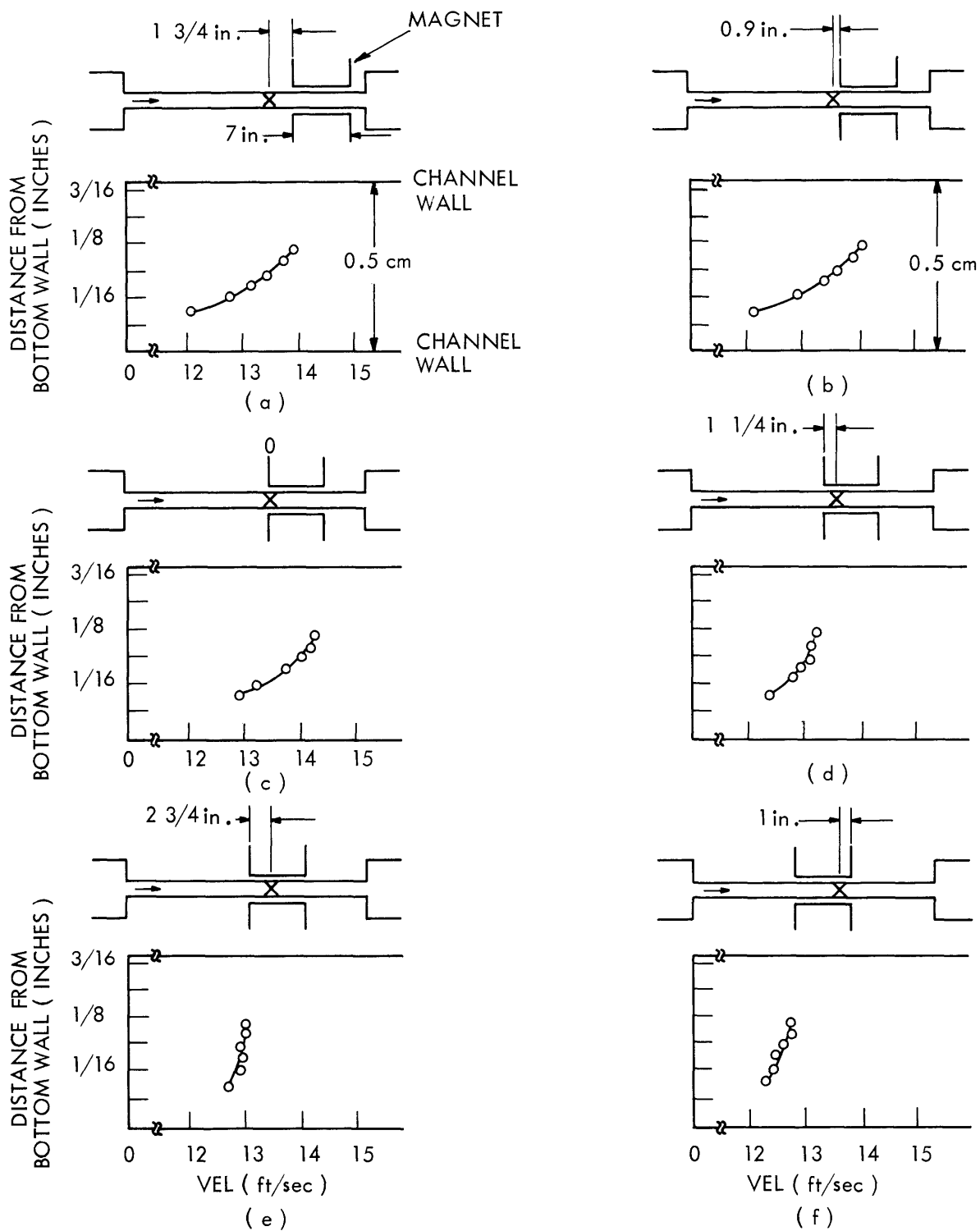
Fig. XII-5. Development of magnetohydrodynamic velocity profile
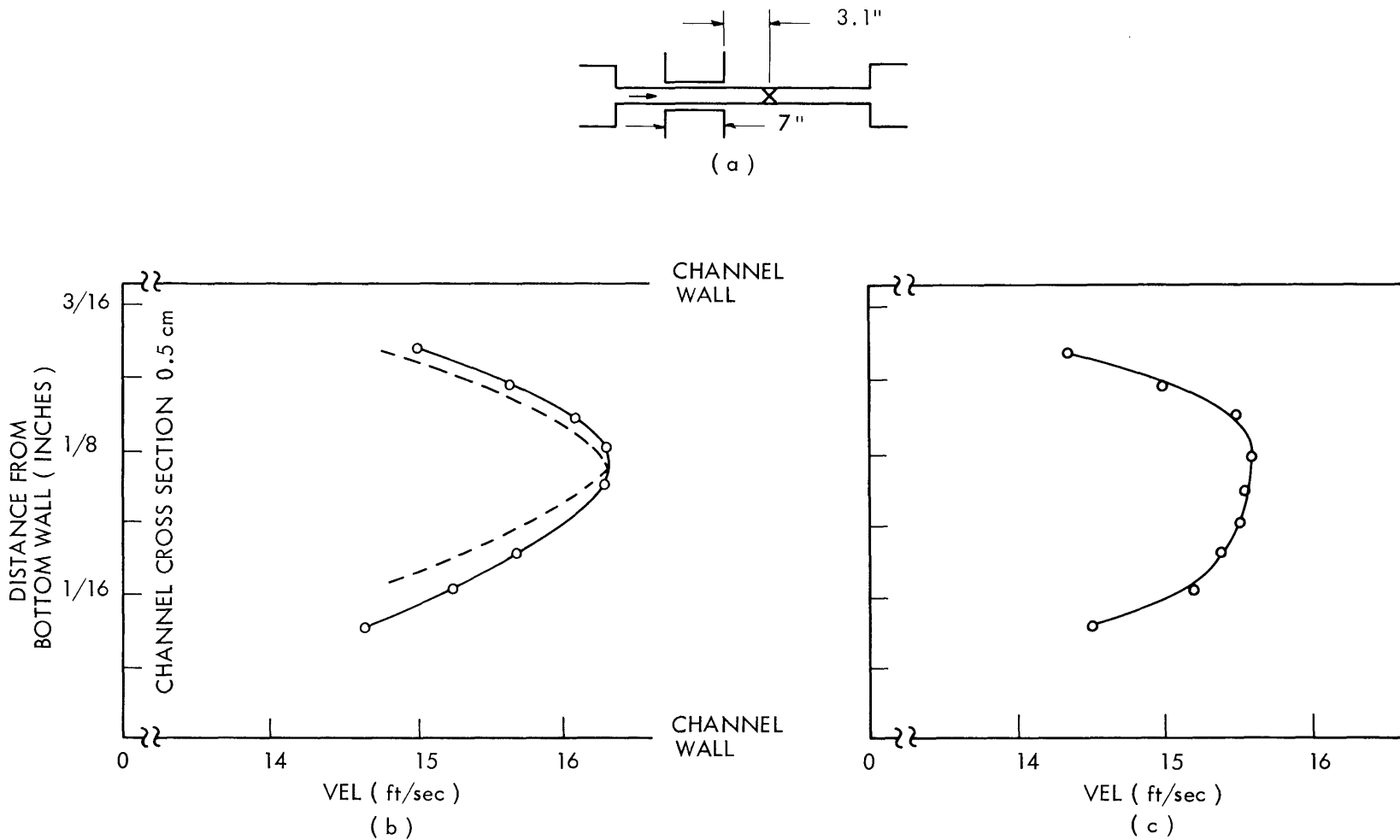($M \approx 66$, $Re \approx 2.9 \times 10^5$).

Fig. XII-6.　Velocity profiles 3.1 inches downstream of field region.　(a) Hg average flow velocity (15.6 ft/sec) from venturi measurements (M = 0 under magnet).　(b) Hg average flow velocity (15.6 ft/sec) from venturi measurements (M = 70 under magnet).

O = Measured values.

- - - = $\frac{1}{7}$ th power law profile with $V_{max} = V_{max\ measured}$

developed turbulent stream of mercury at Reynolds number, $Re \approx 2.9 \times 10^5$, enters a magnetic field region having a Hartmann number, $M \approx 66$, with an MHD entry length of approximately 10 hydraulic diameters. The profile in Fig. XII-5a, with the field downstream of the pitot tube, is similar to the profile measured with no field.

The friction Reynolds number, R^*, based on friction velocity and channel half-height is approximately 4300 for the flow shown in Fig. XII-5. The ratio, M^2/R^*, is approximately 1. Harris[2] computed velocity profiles for turbulent MHD flows. Comparison of our measured profiles with the predicted profiles given by Harris shows qualitative agreement at $M^2/R^* = 1$.

A measured profile at zero field and a computed $\frac{1}{7}$th power law profile are shown in Fig. XII-6a. This profile has been slightly translated to account for probe misalignment. At a similar Reynolds number Fig. XII-6b shows an MHD profile 3.1 inches downstream of the magnetic field region. Some partial ordinary hydrodynamic recovery is observed in the MHD case. In these two flows, with the pitot tube mechanism not obstructed by the magnet, most of the channel could be traversed.

The small channel dimension that was studied, and the necessity of measuring static pressure at the channel wall limited the accuracy of individual profile data. The measurements, however, are adequate for showing the relative rate of profile development. Further work is planned and the preliminary observations reported here provide a clear indication that the MHD flow develops rapidly in a channel of uniform cross section when significant MHD forces are present.

S. Sachs, W. D. Jackson, G. A. Brown

References

1. D. A. East, "The Pitot Tube in a Magnetohydrodynamic Flow," Ph.D. Thesis, Department of Mechanical Engineering, Massachusetts Institute of Technology, September 1964.

2. L. P. Harris, Hydromagnetic Channel Flows (The Technology Press, Cambridge, Mass., and John Wiley and Sons, Inc., New York, 1960).

3. S. Sachs, "Magnetohydrodynamic Entry Lengths as Determined by Pitot Tube Velocity Profile Measurements," S. B. Thesis, Department of Mechanical Engineering, Massachusetts Institute of Technology, June 1965.
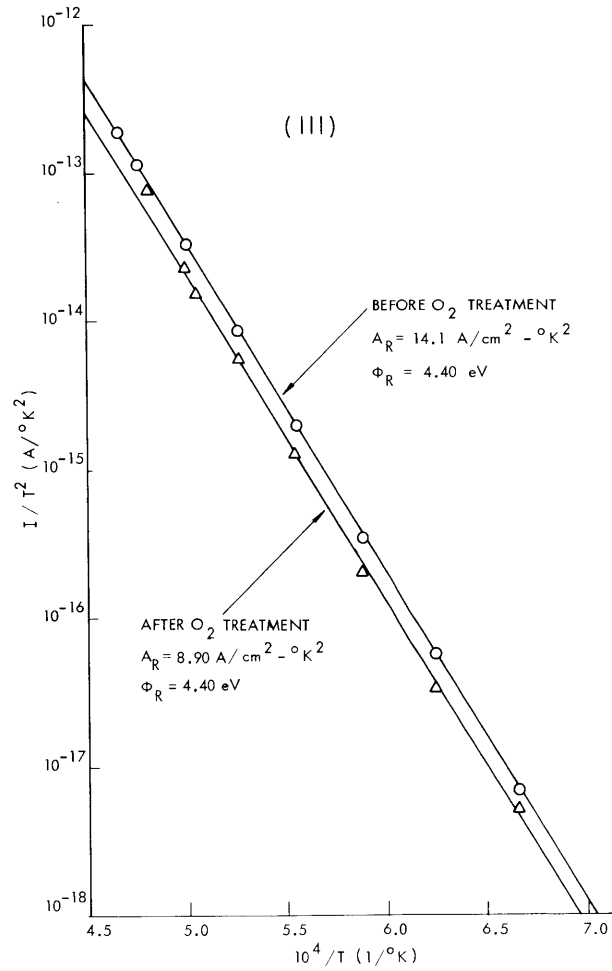
C. THERMIONIC EMISSION FROM A TUNGSTEN MONOCRYSTAL IN OXYGEN

1. Introduction

The purpose of this study is to determine the effect of the carbon impurities in tung-sten filaments on the thermionic properties, and to investigate experimentally the elec-tron emission from a single-crystal tungsten filament as a function of crystallographic direction, filament temperature, and oxygen pressure. Tungsten can be cleansed quite thoroughly because of its refractory properties which allow high flashing temperatures. This does not, however, eliminate the carbon impurities in tungsten. The technique for removing the carbon impurities from tungsten, found by Becker and his co-workers,[1] has been used in this study to find the effects, if any, of carbon on the thermionic emis-sion from tungsten. In a recent study[2] it has been found that the adsorption of cesium on tungsten results in a complete reversal in the form of the emission map. One purpose of the present study is to determine whether or not similar changes take place with adsorbed oxygen.

2. Description of the Apparatus

A schematic diagram of the tube and the circuit used in taking the measurements is shown in Fig. XII-7. The filament is tungsten wire, 7.2×10^{-3} cm in diameter, grown

Fig. XII-7. Schematic diagram of the tube and the circuit used for the measurements.

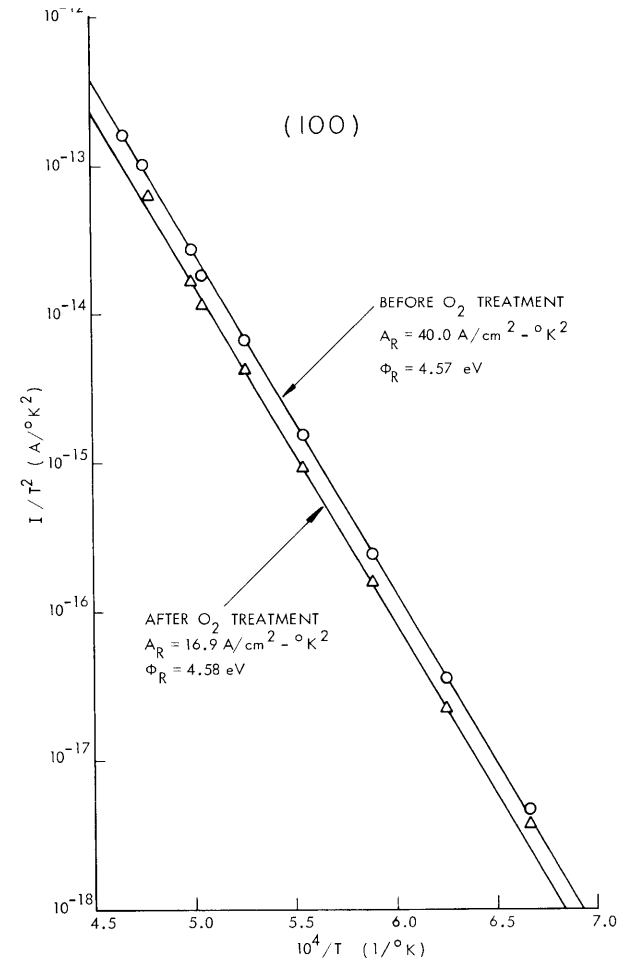Fig. XII-8. Richardson plots for the (111) crystallo-graphic direction in vacuum before and after O_2-treatment.

Fig. XII-9. Richardson plots for the (100) crystallo-graphic direction in vacuum before and after O_2-treatment.

into a single crystal and mounted in the center of the tube. It is surrounded by a concentric tantalum anode, 2 cm in diameter, with a slit, 0.75 mm wide and 1 cm long. This slit which subtends an angle of 4.30° on the filament, enables the electrons emitted from an area of 2.7×10^{-4} cm^2 on the crystal to reach a collector. The collector, a nickel cylinder, 3 cm in diameter, is covered with platinum black on the inside in order to reduce electron reflection. Two iron slugs mounted on the anode permit rotation of the slit from outside the tube by using magnets. To take the emission maps, the anode and the collector were biased 1 kv and 4 v positive with respect to the filament, respectively.

3. Results

The work functions obtained in vacuum for the (111) and (100) directions compare well with data obtained by Nichols,[3] Smith,[4] and Coggins.[2] The vacuum measurements, including collector and anode bias data, Schottky and Richardson plots, and an emission map of the tungsten crystal, indicated a satisfactory condition of test tube and filament.

Following Becker's[1] technique to remove the carbon impurities from the filament, the tungsten filament was held at 2200°K in oxygen at 1×10^{-6} torr for 63 hours. Figures XII-8 and XII-9 show Richardson plots with the collector current reduced to zero
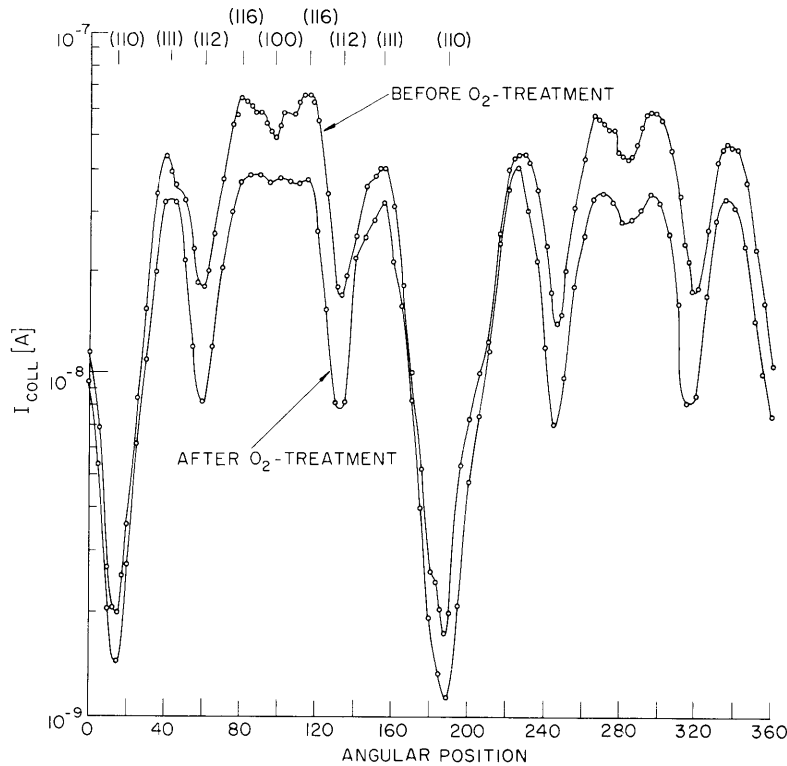

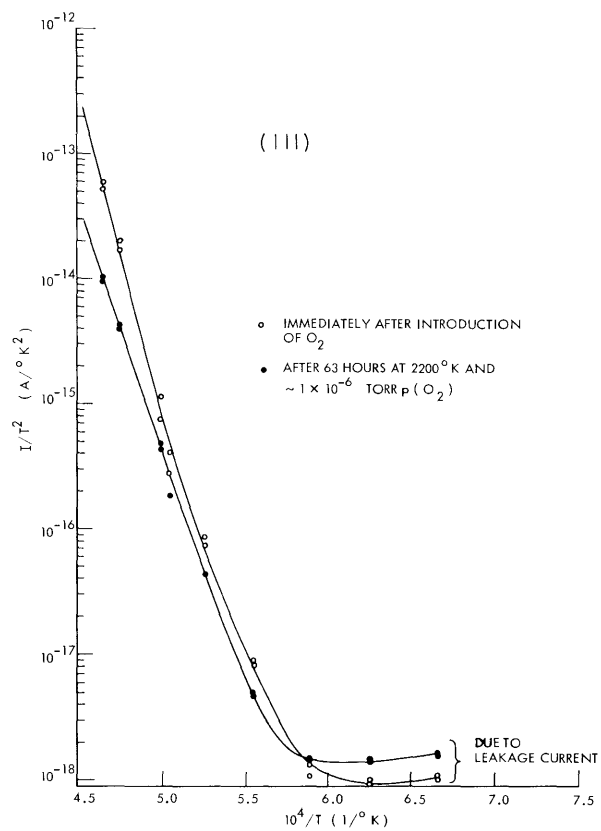Fig. XII-10. Emission maps for 1900°K before and after O_2-treatment in vacuum.

Fig. XII-11. Richardson plots for the (111) crystallographic direction in 1×10^{-6} torr oxygen before and after O_2-treatment.
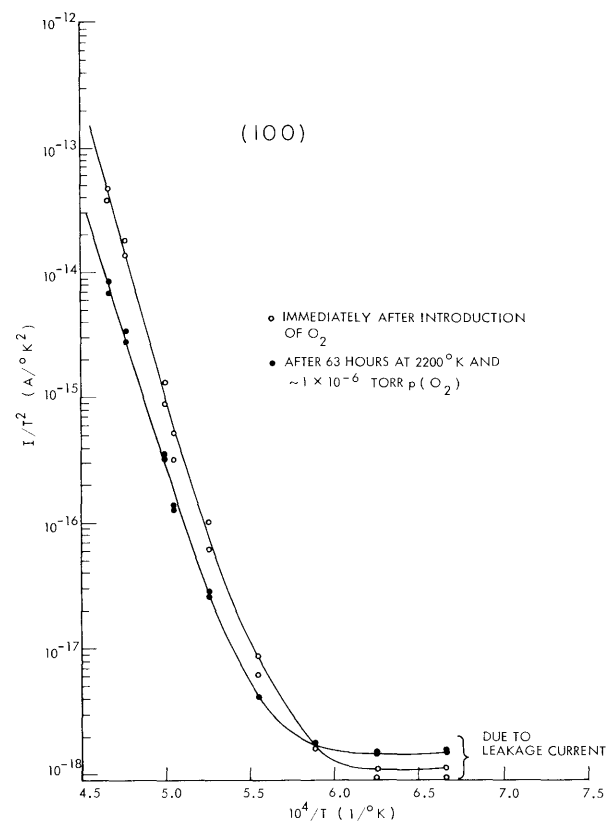
Fig. XII-12. Richardson plots for the (100) crystallographic direction in 1×10^{-6} torr oxygen before and after O_2-treatment.

field for the (111) and (100) directions taken in vacuum before and after the treatment with oxygen. For both crystallographic directions the Richardson work functions, ϕ_R, remained the same, but the Richardson constants, A_R, decreased. This decrease in emission appears also in the vacuum emission maps for a 1900 °K filament temperature taken before and after the O_2-treatment (Fig. XII-10). A comparison of the two emission maps also shows marked differences in the vicinity of the (100) crystallographic directions. The difference between the (116) and the (100) directions has greatly diminished, even though the emission in the (100) direction is still less than in the (116) crystallographic direction. These differences could be due to lattice rearrangements, as suggested by Ehrlich.[5]

Richardson plots for the (111) and (100) crystallographic directions taken in oxygen at ~1 $\times$ 10^{-6} torr before and after the 63-hour oxygen treatment of the filament are shown in Figs. XII-11 and XII-12. Here too, the decrease in emission is apparent; however, the Richardson plots are now curves instead of straight lines with the tangents indicating an increasing work function for increasing temperature. This seems to be a transition Richardson plot, as suggested by Johnson and Vick,[6] in the region between half and full coverage. A meaningful Richardson plot from which the work function can be determined cannot be obtained by this method, since the surface coverage varies with filament temperature.

Richardson plots taken in $p(O_2)$ = 1 $\times$ 10^{-8} torr appear to be the same as the plots taken in vacuum. The close similarity of the emission maps shown in Figs. XII-13 and XII-14 indicates that an oxygen pressure of 1 $\times$ 10^{28} torr has no significant effect upon the emission from a tungsten filament at temperatures above 1500 °K.

Emission maps taken at various oxygen pressures and filament temperatures are shown in Figs. XII-13 through XII-16. In comparison, these show that, in addition to the expected decrease of the electron emission, the contrast between the emission in the (111) direction and that in the (100)-(116) range decreases with increasing oxygen pressure and decreasing filament temperature, that is, with increasing oxygen coverage of the tungsten filament. A similar decrease in contrast is observed for the (112) and (110) directions; in fact, the emission in the (112) direction becomes less than the emission in the (110) direction at T_{Fil} = 1900 °K in $p(O_2)$ = 1 $\times$ 10^{-7} torr. Similarly, the relative magnitudes of the electron emission in the (100) and (116) directions reverse at the higher oxygen pressures. A possible explanation for these phenomena could be found in a preferential affinity of the oxygen for different crystallographic faces.

Figure XII-17 shows the effective work functions ϕ_E as functions of filament temperature for the various oxygen pressures and crystallographic directions. In principle, it should be possible to present these data on a plot of ϕ_E against coverage θ. We have not been able to do this because it is not possible to determine the coverage in this experiment and appropriate reliable data do not exist for single crystals.
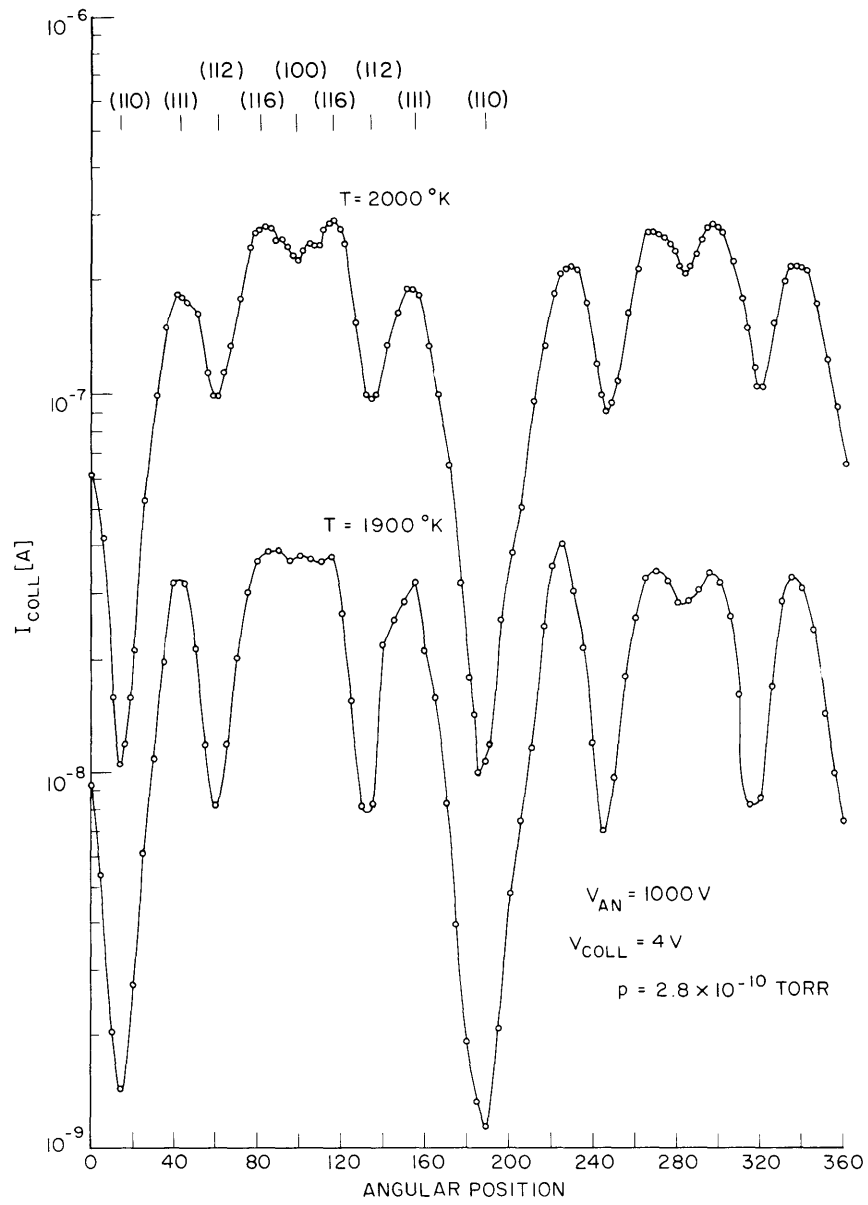
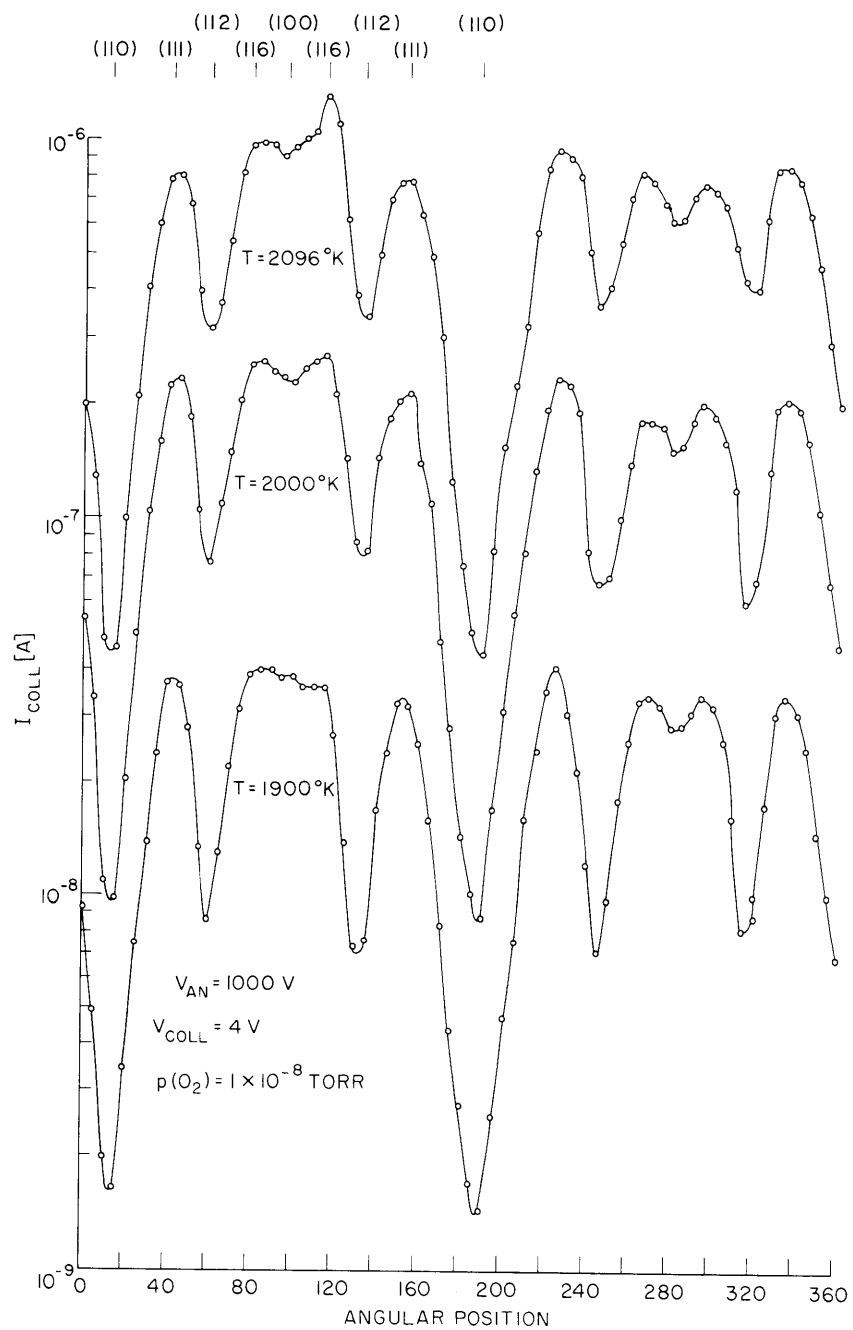Fig. XII-13. Emission maps in vacuum.

Fig. XII-14. Emission maps in oxygen at 1×10^{-8} torr.
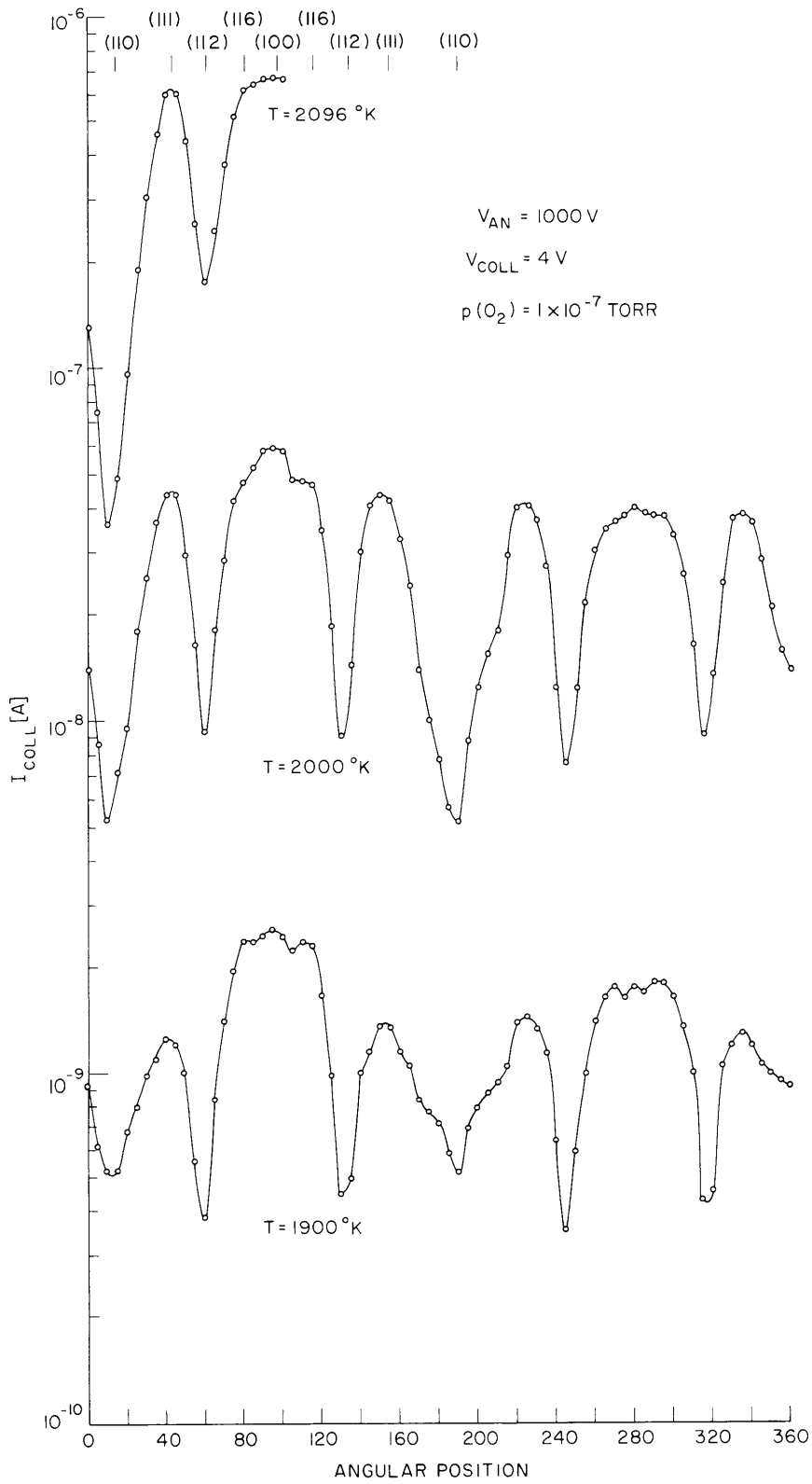
Fig. XII-15. Emission maps in oxygen at 1×10^{-7} torr.
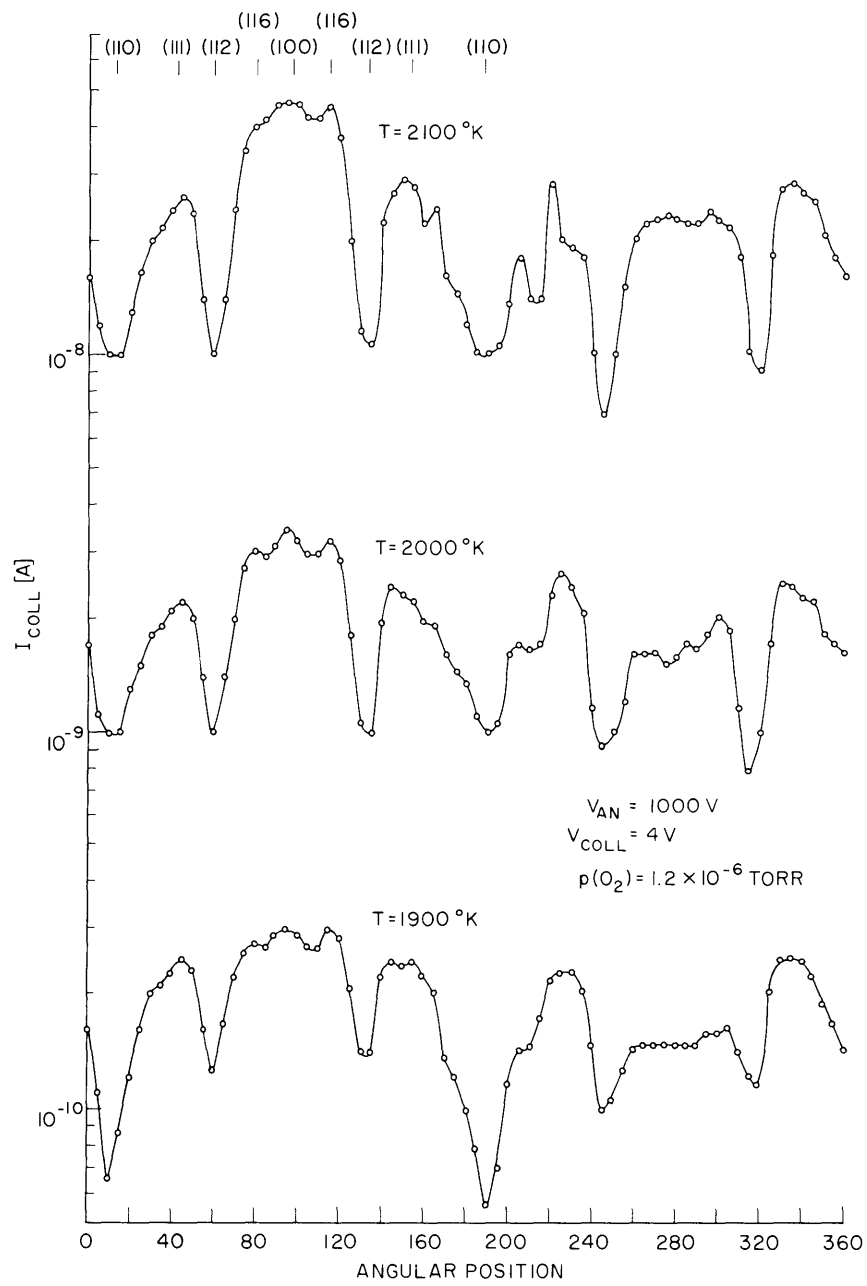
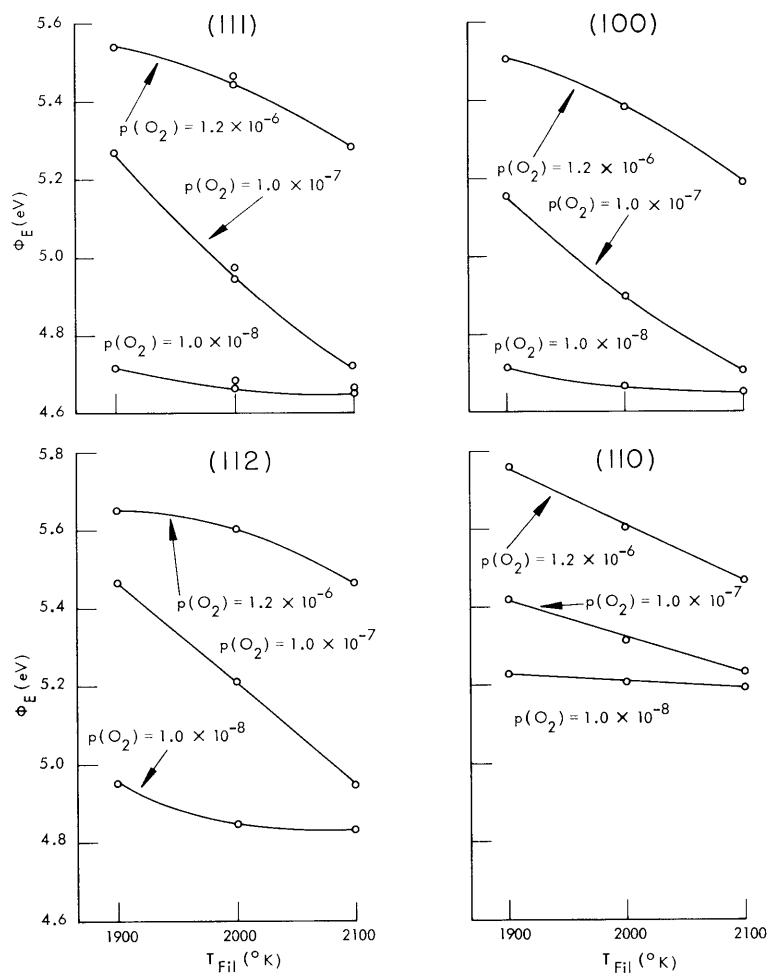Fig. XII-16.   Emission maps in oxygen at 1.2×10^{-6} torr.

Fig. XII-17. Effective work function of different crystallographic directions as a function of filament temperature and oxygen pressure.
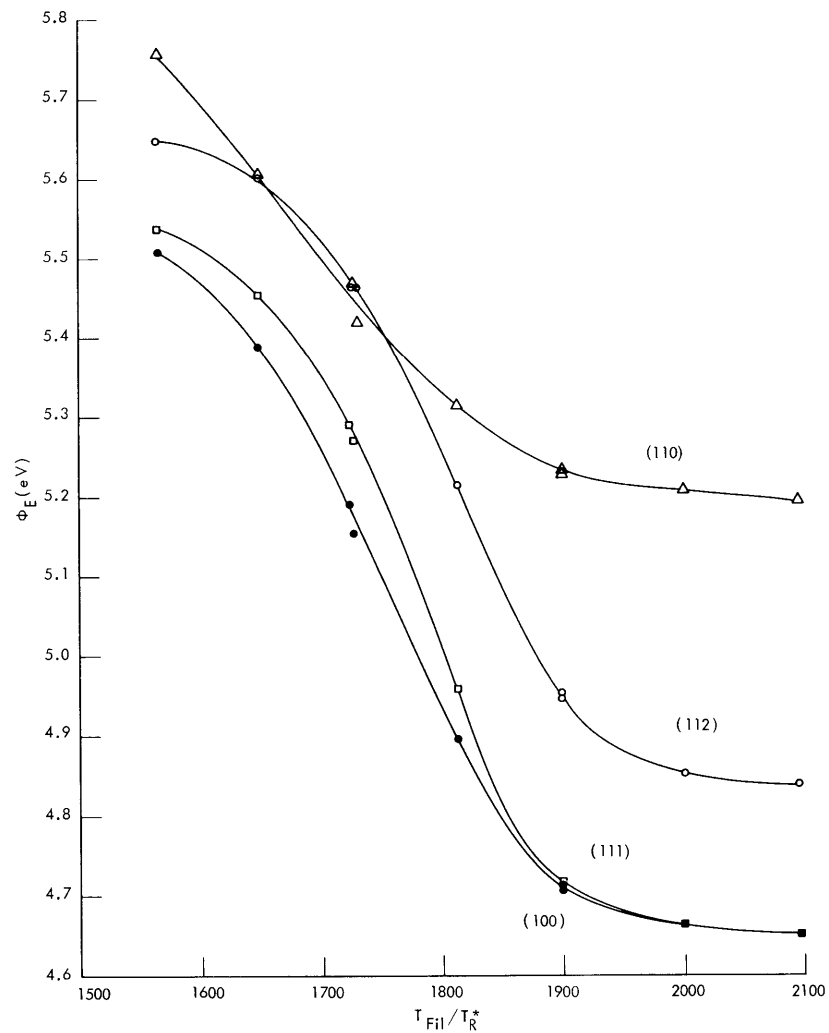
Fig. XII-18. Effective work function vs the ratio of filament temperature to effective reservoir temperature for various crystallographic directions.

An attempt to find an empirical parameter related to the coverage was quite successful, as shown in Fig. XII-18. The effective reservoir temperature T_R^* used in this parameter, T_{Fil/T_R^*}, is defined as

$$T_R^* = 1 + 0.0447 \ln \frac{p}{1 \times 10^{-8}}, \tag{1}$$

where p, the oxygen pressure, is in torr. Although no definite significance can be ascribed to the exact value of T_R^*, the curves in Fig. 3.3.12 are quite similar to the ϕ_E versus T/T_R plots for cesium on tungsten (for example, see Rasor and Warner[7]).

By comparing Figs. XII-13 through XII-16 it was previously found that the relative positions of the (110) and (112) directions reverse at $T_{Fil} = 1900°K$ and $p(O_2) = 1 \times 10^{-7}$ torr, which corresponds to $T_{Fil/T_R^*} = 1726$; this is also clearly shown in the overlapping of the curves for these crystallographic directions between $T_{Fil/T_R^*} = 1656$ and 1750. The variation of the (111) and (100) directions relative to each other is also obvious.

A strong decay in the electron emission, especially in an oxygen atmosphere, made flashing the filament at short intervals necessary. The breakage of the filament terminated any further investigation.

4. Summary

We found that the carbon impurities do not influence the work function of tungsten. The Richardson constant decreases slightly after the oxygen treatment. Adsorption of oxygen produces the expected decrease in emission, but the changes are not as strongly dependent on crystallographic direction as for cesium on tungsten.[2]

W. Engelmaier, R. E. Stickney

References

1. J. A. Becker, E. J. Becker, and R. G. Brandes, J. Appl. Phys. 32, 411 (1961).
2. J. L. Coggins, Ph.D. Thesis, Department of Mechanical Engineering, Massachusetts Institute of Technology, 1965.
3. M. H. Nichols, Phys. Rev. 57, 297 (1940).
4. G. F. Smith, Phys. Rev. 94, 295 (1954).
5. G. Ehrlich, Ann. N.Y. Acad. Science 101, 722 (1963).
6. M. C. Johnson and F. A. Vick, Proc. Roy. Soc. (London) A158, 55 (1937).
7. N. S. Rasor and C. Warner, J. Appl. Phys. 35, 2589 (1964).

D. CHARACTERISTICS OF A PURE ALKALI-METAL VAPOR PLASMA

The alkali vapor has been studied as a multicomponent system in which aggregates
of atoms and electrons are characterized by a mass factor g and a charge factor Z, the
mass of the aggregate being equal to g times the mass m_a of an atom and its charge to
Z times the absolute value of the electron charge. As we deal with states out of thermo-
dynamic equilibrium, a kinetic approach is used for which distribution functions f_g^Z are
defined, their space and time evolution being governed by equations of the Liouville type.
Collisional effects are exhibited in the usual way, with correlations between velocity and
position for particles neglected. This limits us to densities for charged particles low
enough so that the 90° Coulomb impact parameter is much smaller than the mean dis-
tance between particles. For aggregates consisting of a large enough number of atoms
(approximately 10), the liquid-drop model[1,2] is used. Furthermore, all collisions
except drop-drop collisions are taken into account. Finally, we limit ourselves to large
Knudsen numbers based on the size of the particles, but small Knudsen numbers based
on the characteristic length of the phenomenon under study. The study of the collisions
with drops is done in the length scale characterizing the "range" of such interactions,
and taking a Maxwellian as a first approximation to the electron, ion and atom distribu-
tion functions. Taking successive moments of the Boltzmann equations, the evolution
of these moments is found (on a length scale much larger than the one characterizing
the collisional operators). From such an analysis a generalization of the condensation
and of the nonequilibrium ionization theories resulted.

1. Condensation

It has been found that below degrees of ionization of approximately 2 per cent the
classical nucleation theory[1,2] applies. At pressures of ~1/100 of an atmosphere, a
critical supersaturation ratio of ~5 is found.

For higher degrees of ionization, the drops will tend to be negatively charged,
thereby increasing the number of ions condensing per unit surface and the time by a
factor of s_i, which can be as high as 50 for small drops of nucleation size. An effective
supersaturation ratio then has to be introduced which will be expressed by

$$(S_a)_{eff} = S_a \left[1 + \frac{(s_i-1)N_i}{N_a + N_i} \right],$$

where S_a is the classical supersaturation ratio, N_i and N_a the ion and atom number den-
sities. For N_i/N_a = 2 per cent, it is seen that $(S_a)_{eff}/S_a$ is approximately 2.

Given a supersaturation ratio, the critical size for nucleation is also decreased,
because of the electrostatic pressure term. This effect is less important, however, than
the preceding effect. The drop growth is, as usual, limited by heat transfer from the

drops. In particular, for very high electron densities, the growth rate is further reduced because of the energy released by ion-electron recombination on the drop.

2. Ionization

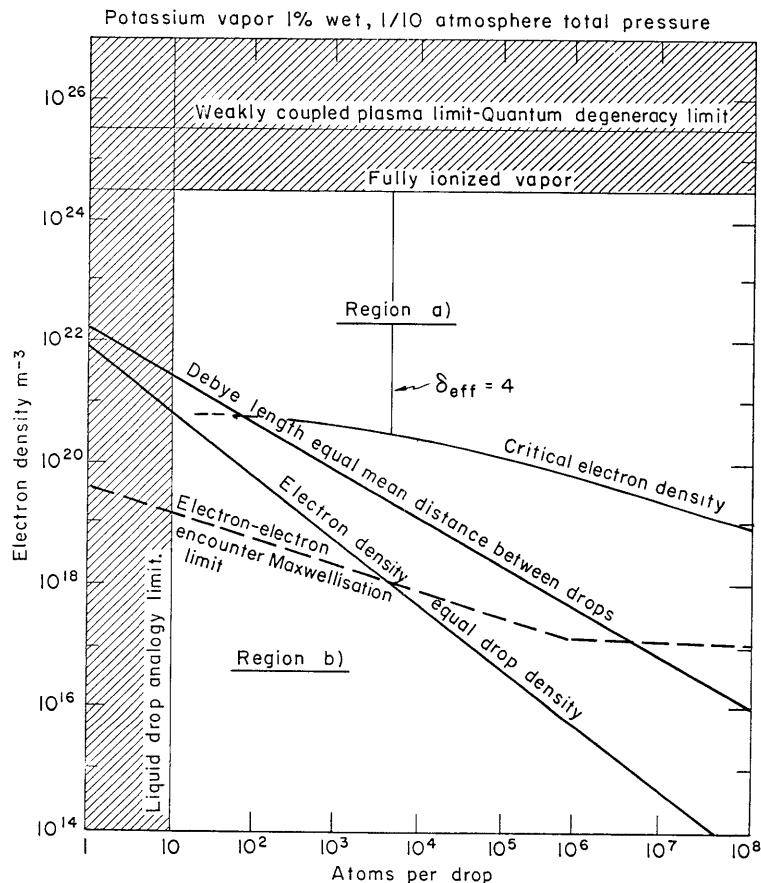For a given degree of moisture, two important plasma regimes can be identified, as shown in Fig. XII-19.

Fig. XII-19. Plasma regime classification for wet potassium vapor.

High electron densities: When the mean distance between drops is much larger than the Debye shielding length, most of the plasma consists of a region in which the electron and ion densities are equal. Drops are shielded from each other by sheaths.

Low electron densities: The Debye length is much larger than the mean distance between drops, so that an electron interacts simultaneously with a large number of them. In Fig. XII-19 the limits for the liquid-drop model are presented, as well as those for the Maxwellization of the electron distribution function through electron-electron encounters.

For high electron densities the rate at which drops charge is much faster than their evolution in size. Hence, at every instant an equilibrium distribution with charge can be assumed for the drops, together with an ionization equilibrium.

The study of the steady-state distribution of drops with charge shows that they will be predominantly negative in charge, the steady-state regime being reached when the number of electrons and ions condensing per unit time is equal. This leads to a decrease in the electron condensation rate by a factor which for potassium at 1/100 atmosphere is ~30, and the ion condensation rate increases by a factor $s_i \approx 10$. The right-hand side of the continuity equation for electrons is then set equal to zero so that

$$R_{ioniz}N_e\left[(N_e)^2_{Saha}-N^2_e\right] + N_D 4\pi\overline{R^2}s_i \sqrt{\frac{kT_a}{2\pi m_a}} \left(N^*_i - N_e\right) = 0.$$

Here, we have supposed atom ionization by electron impact and three-body recombination in the presence of an electron, $(N_e)_{Saha}$ being the local electron density as evaluated through the Saha equation at the local electron temperature, and R_{ioniz} an ionization rate constant evaluated by Byron and his co-workers[3] for potassium, which is a function of the electron temperature. N_D is the drop number density, $4\pi R^2$ their mean physical surface, T_a the atom temperature, and N^*_i has the dimension of a number density and characterizes ion evaporation from drops.

For a dry vapor, $N_D = 0$, so the $N_e = (N_e)_{Saha}$, as expected from Kerrebrock's two-temperature model theory.[4] For a wet vapor, it is convenient to set

$$\eta_e = \frac{N_e}{(N_e)_{Saha}} \qquad \eta_i = \frac{N^*_i}{(N_e)_{Saha}}$$

$$K = \frac{(4\pi\overline{R^2})s_i N_D \sqrt{\frac{kT_a}{2\pi m_a}}}{R_{ioniz}(N_e)^2_{Saha}} = \left(\frac{\mu}{\overline{R}}s_i\right) f(T_e),$$

where the gas temperature is supposed to remain constant, and μ is the degree of moisture defined as

$$\mu = \frac{N_D\overline{g}}{N_a}.$$

The term η^*_i in general is very small for the vapor pressures (and hence temperature) that we shall consider (approximately 10^{-6}), so that the continuity equation which is now written

$$1 - \eta_e^2 = K\left(1 - \frac{\eta_i^*}{\eta_e}\right)$$

has the following solutions

$$K < 1 \qquad \eta_e^2 \cong 1 - K$$

$$K > 1 \qquad \eta_e \cong \eta_i^*\left(\frac{K}{K - 1}\right) \ll 1.$$

The transition from one solution to the other as K goes through the value of one is very sharp as exhibited in Fig. XII-20, which represents an evolution at constant electron temperature and constant mean radius, the degree of moisture being variable. This
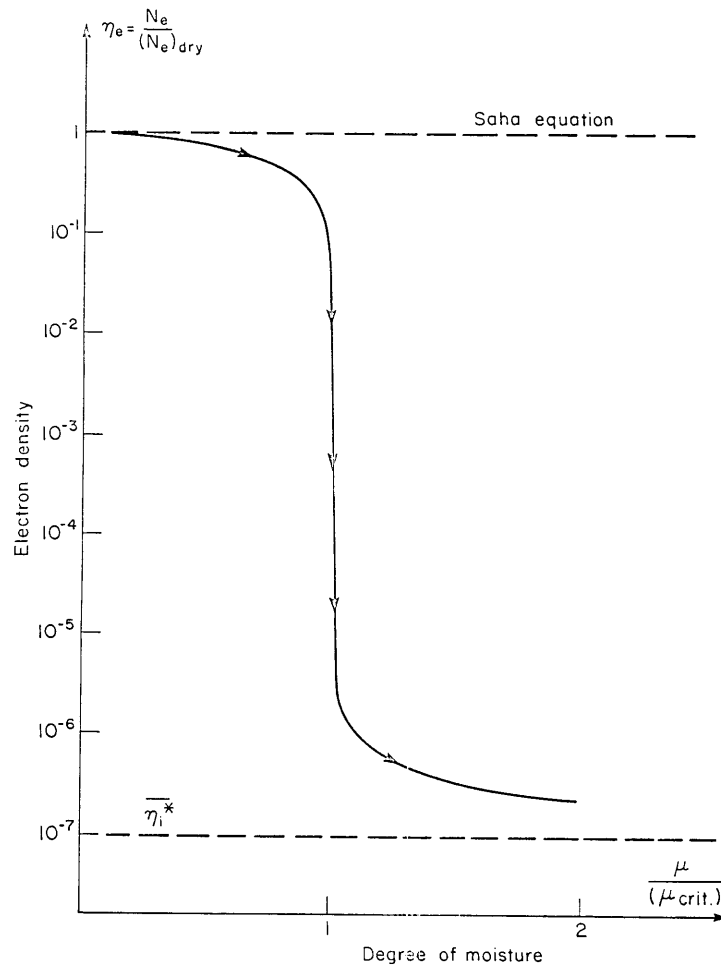

Fig. XII-20. Typical electron density variation with degree of moisture at constant electron temperature and mean drop size.

behavior can be stated in the following way. Given an electron temperature and a mean drop size, there exists a critical degree of moisture above which nonequilibrium ionization cannot be sustained. (We may also alternatively for a given degree of moisture, drop radius, and pressure define a critical electron density; this is represented in Fig. XII-19.) The condition under which an electron temperature can be maintained above the gas temperature can be found through the energy equation which is written, where J is the current density and σ the electrical conductivity,

$$\frac{J^2}{\sigma} = \delta \frac{m_e}{m_a} N_e (N_a Q_{ea} + N_i Q_{ei}) \sqrt{\frac{8kT_e}{\pi m_e}} \frac{3}{2} k(T_e - T_a) + N_D 4\pi \overline{R^2} s_i \sqrt{\frac{kT_a}{2\pi m_a}} N_e (eV_i) + Q_R.$$

Here, the joule heating is seen to be balanced by the energy loss terms. The elastic energy loss with atoms and ions is represented by the first term on the right-hand side. The second term represents the inelastic energy loss due to electron-ion recombination on drops (V_i is ionization potential), and the last term represents the energy loss by
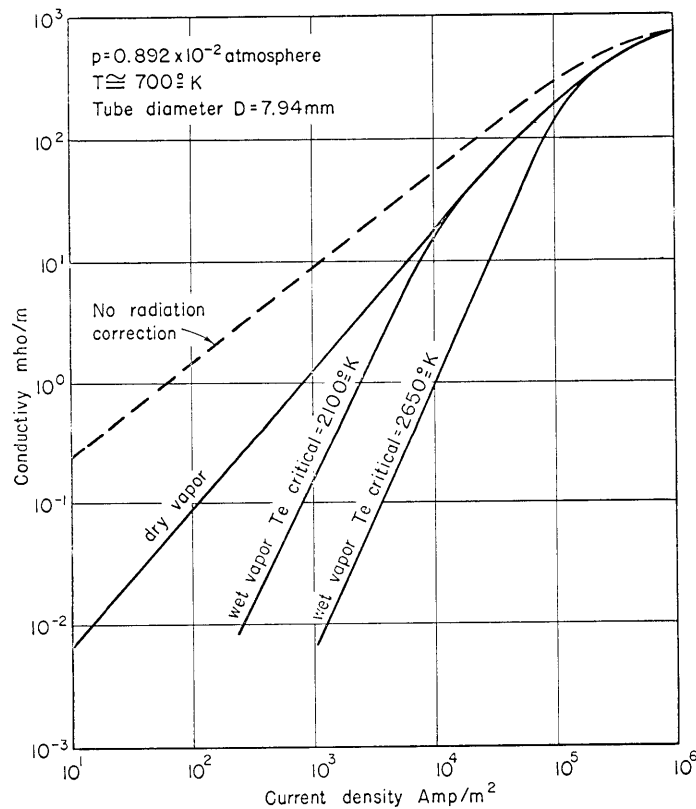

Fig. XII-21. Electrical conductivity of dry and wet potassium vapor vs current density ($\delta_{eff} \sim 2$).

radiation. For a monatomic alkali metal vapor δ is equal to 2.

As the first and second terms on the right-hand side are proportional to the electron density, N_e, an effective energy loss parameter δ_{eff} can be defined so as to put the inelastic drop losses in a form comparable to the elastic losses. The value $\delta_{eff} = 4$ corresponds to equality of the two terms and is represented in Fig. XII-19. This was selected as a reasonable maximum allowable value for an MHD generator.

With this model, it has been shown that for the degrees of moisture considered here (a few per cent), the total cross section for momentum exchange between electrons and drops is much smaller than the cross section with atoms and ions. Hence, changes in conductivity will be due primarily to changes in electron density, and the Hall parameter is practically unaffected by condensation.

The expected behavior of σ versus current density J is presented in Fig. XII-21. The branches corresponding to the departure from the dry state have a slope equal to 2 on the log (σ) vs log (J) plot. This is due to the fact that as K approaches 1, the electron temperature on this branch remains almost constant but the electron density decreases. This causes both elastic and inelastic losses to decrease so that the energy equation for these branches is approximately

$$\frac{J^2}{\sigma} = Q_R = \text{constant.}$$

This remains valid as long as the first two excited states for atoms, which give most of the contribution to the radiation term, are in equilibrium at the electron temperature.

3. Experimental Results

Experiments were conducted for a dry potassium vapor. The experimental apparatus has been described in a previous report,[4] in which Hall parameter measurements were seen to be in good agreement with the theoretical predictions based on a cross section of 250 Å for potassium. More refined electrical conductivity measurements were made for the dry vapor. Some characteristic results are presented in Fig. XII-22. The agreement with theory is seen to be quite good except at high current densities for which, owing to the low pressure (1/100 atm), the joule heating of the gas is quite important. At very low current densities, the measured electrical conductivity is abnormally high. This has been reported elsewhere[5] in connection with electrical conductivity measurements of argon-seeded plasmas.

For a wet vapor, due to the fact that the kinetics of condensation at this pressure is very slow, condensation was started before the test section entrance. Supersaturation ratios as high as 7 have been observed, in the absence of ionization, which suggest that nucleation in this case is correctly predicted by the classical nucleation theory.[1,2]

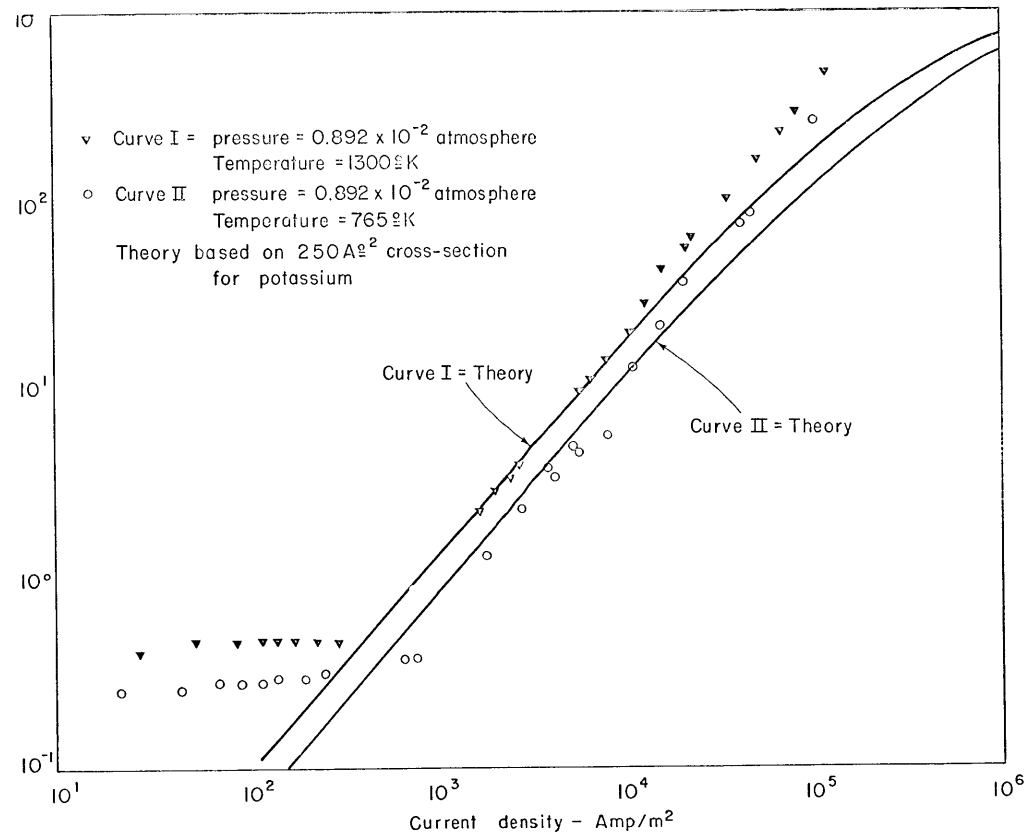Measurements of electrical conductivity in a wet vapor are difficult because of the
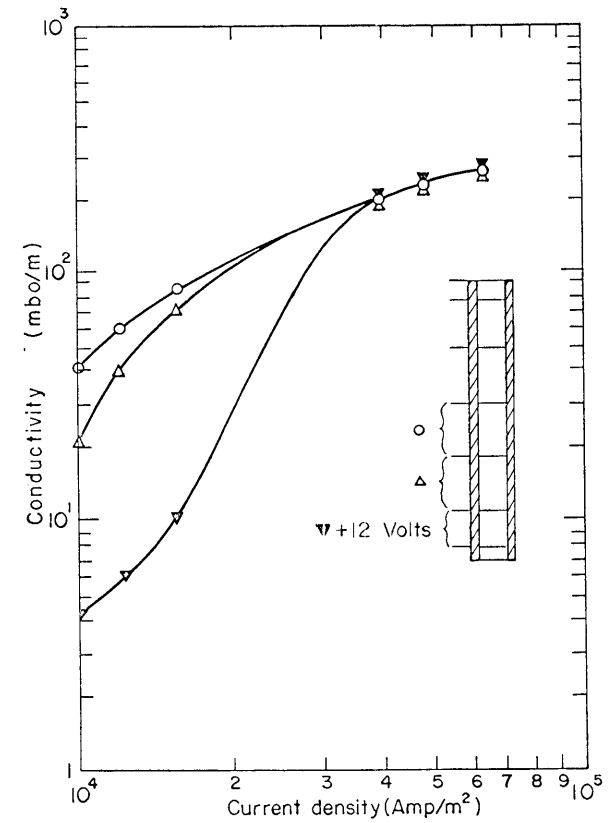
Fig. XII-22. Dry potassium vapor electrical conductivity.

Fig. XII-23. Wet potassium vapor conductivity at different test section locations.

joule heating of the gas which at high current densities tends to evaporate the drops. At current densities of ~1 amp/cm^2, the voltages at the inlet of the test region increased because of the effect of condensation. Only a semiquantitative comparison with theory can be made by plotting the average electrical conductivities in the interprobe space. This has been done and is presented in Fig. XII-23, in which a good qualitative agreement with theory is seen to exist (compare with Fig. XII-21).

J. L. Kerrebrock, M. A. Hoffman, A. Solbes

References

1. J. Frenkel, Kinetic Theory of Liquids (Clarendon Press, Oxford, 1946).

2. P. Hill "Homogeneous Nucleation of Supersaturated Water Vapor in Nozzles," Report No. 78, Gas Turbine Laboratory, Massachusetts Institute of Technology, Cambridge, Massachusetts, January 1965.

3. S. Byron, et al., "Electron-Ion Reaction Rate Theory," Proc. Fourth Symposium on Engineering Aspects of Magnetohydrodynamics, University of California, Berkeley, April 1963.

4. J. L. Kerrebrock, M. A. Hoffman, and A. Solbes, "Behavior of Dry Potassium Vapor in Electric and Magnetic Fields," Quarterly Progress Report No. 77, Research Laboratory of Electronics, M.I.T., April 15, 1965, pp. 232-237.

5. J. L. Kerrebrock, "Nonequilibrium Ionization due to Electron Heating, I and II," AIAA J. 2, 1072-1087 (June 1964).

E. BRAYTON CYCLE MAGNETOHYDRODYNAMIC POWER GENERATION

The research reported here was undertaken to obtain a thorough understanding of closed Brayton cycle MHD power generation and to provide data for comparison with other competitive power generation techniques. The current state of the art in magnetics, reactor design, and high-temperature materials technology has fixed upper limits on the operation of the cycle and its components. Results of the analysis indicate the feasibil- ity of the cycle for terrestrial applications. The MHD Brayton cycle is not competitive with Rankine cycle systems now in operation, because of large refrigeration require- ments necessary for operation of superconducting coils that provide the generator's mag- netic field.

1. Brayton Cycle Magnetohydrodynamic Power Generation

A detailed analysis has been undertaken to determine the feasibility of closed Brayton cycle magnetohydrodynamic power generation.[1] The two primary constraints on such a system — the maximum available stagnation temperature from the heat source, and the minimum generator exit temperature below which efficient power generation is impos- sible — have been determined in the light of current technological capabilities.

Operating with a maximum stagnation temperature in the range of 1500°K from a gas-cooled nuclear heat source requires nonequilibrium conductivity considerations for the working fluid. The coupled working fluid requirements of compatibility with a nuclear environment and satisfactory electrical conductivity (in excess of 100 mhos/meter) result in the selection of neon seeded with cesium as the working fluid. Heat-transfer considerations would favor a helium-cesium mixture; however, the electrical conductiv- ity of this mixture is unsatisfactory at operating pressures of approximately 15 atm which yield acceptable heat transfer areas in the heat source and sink.

Cycle operation with the neon-cesium mixture is feasible with the indicated maximum stagnation temperature and current density levels of $1.0 \cdot 10^5$ to $3.0 \cdot 10^5$ amps/m^2 in the MHD generator. The magnetic field intensities necessary to sustain these current density levels range from 7.5 to 20 webers/m^2, and thus require superconducting coils. The minimum cycle heat-rejection temperature is in the range 300-400°K, with the result that space application of this system would be unsatisfactory. The heat-rejection temper- ature is too low for efficient utilization of space radiators. Terrestrial operation of the system is feasible with cycle efficiencies in the range 39-49%. The analysis yielding this range of efficiency has considered viscous dissipation in the high velocity flow through the MHD generator, nonisentropic operation of the cycle diffuser and compres- sor, and utilization of the rejected heat as the heat source for a secondary cycle. Power from this secondary cycle must be utilized to drive the Brayton cycle compressor, since the compressor power is a significant fraction of the electric power output, and cannot

be efficiently supplied from the primary Brayton cycle. Additional restrictions on this analysis include operation of the secondary cycle at an efficiency of 40%, and neglect of power requirements for refrigeration of the superconducting coils.

Although the analysis indicates feasibility of the MHD Brayton cycle, the system is not competitive with Rankine cycle systems using water as the working fluid and operating conventional generators. The unattractiveness of the MHD system stems from the low electrical conductivity of the working fluid at thermodynamic states compatible with available heat sources. As a result, high levels of the applied magnetic field are required, sustainable only with superconducting coils. The refrigeration requirements for such coils degrades the otherwise acceptable cycle efficiency to an uncompetitive level.

C. A. McNary

References

1. C. A. McNary, M. E. Thesis, Department of Mechanical Engineering, M.I.T., 1965.